IEEE Robotics and Automation Letters (RA-L) paper, presented at ICRA 2026, Vienna, Austria. Cite as RA-L paper.

Polarization-Controlled Microwave-Actuated Continuum Robot

Yongze Li, He Gao, Zhiguang Xing, Xuan Li, and Tao Chen

***Abstract*—In industrial and medical environments, robotic manipulation frequently encounters dual challenges of spatially constrained workspaces and visual obstructions. Wireless actuation methodologies, leveraging non-contact energy transmission and adaptive control mechanisms, offer an innovative solution to address the limitations of physical interconnections and enhance operational adaptability in structurally confined and uncertain obstructed environments. Here, we implemented a non-contact continuum robotic arm based on microwave-driving with polarization-directed guidance. The system incorporates customized flexible printed circuit (FPC) antennas and spatial microwave energy field modulation to enable wireless actuation and multi-degree-of-freedom (DOF) motion control of the robotic end-effector. By integrating spring-supported mechanisms and shape memory alloy (SMA) spring deformation responses, it accomplishes tasks such as obstacle penetration, component grasping, and retrieval—all without physical connections. This study demonstrates precise coupling between directionally controlled microwave energy and mechanical motion in obscured settings, offering a novel approach for non-contact, multi-DOF, and multi-structure robotic operations in sealed or unstructured environments. The proposed methodology significantly expands the potential applications and operational capabilities of robots in complex real-world conditions.**

***Index Terms*—Actuation and joint mechanisms, soft robot applications, modeling, control, learning for soft robots.**

I. Introduction

IN BOTH traditional industrial and medical settings, robotic arms often face dual challenges of structurally constrained spaces and uncertain obstructed environments, particularly when target objects are located in visually occluded areas or require delicate operations through complex obstacles. Conventional rigid robotic arms, due to their structural limitations, struggle to achieve effective non-contact intervention in such scenarios. Thus, continuum robotic arms have emerged as a promising solution for operations in confined and unstructured environments, owing to their high compliance, multi-DOF maneuverability, and adaptable configuration modulation capabilities [1], [2], [3], [4]. However, their actuation mechanisms predominantly rely on physical transmission systems such as cable-driven or pneumatic approaches, which often result in bulky system architectures and inherent dependence on physical connections. These limitations considerably restrict their penetration capability and adaptability in densely obstructed workspaces.

To overcome the limitations of physical transmission mechanisms, various contactless actuation methodologies have demonstrated distinct application potentials due to their unique operating principles. Acoustic manipulation excels in liquid environments, enabling non-destructive handling of biological cells and microscopic particles [5], [6], [7], [8]; optical driving exhibits unique advantages in vacuum or transparent media, enabling long-range high-precision optical manipulation [9], [10], [11], [12]; magnetic actuation proves particularly suitable for in vivo applications, offering ideal solutions for targeted drug delivery and magnetically controlled microrobots [13], [14], [15], [16], [17]. Microwave-driven actuation, leveraging the unique properties of electromagnetic waves, enables physical separation of the power source and wireless energy transfer in confined spaces. Furthermore, its strong penetration capability through non-metallic obstacles (such as plastics, acrylic, wood, and cardboard) demonstrates the potential to deliver energy to concealed targets through non-metallic barriers [18], [19], [20], significantly expanding its application boundaries in obstructed scenarios (i.e., environments with physical blockages) [21]. With advantages including far-field transmission capability, strong directivity, and independence from the magnetic properties of manipulated objects, these features render microwave-driven actuation particularly suitable for implementing contactless robotic manipulation in industrial obstructed environments.

In recent years, microwave actuation technology has evolved from fundamental energy transmission to enabling precise manipulation and control of micro-scale devices. Researchers have achieved non-contact manipulation of millimeter-scale objects through the development of novel microwave-sensitive material architectures and optimized antenna radiation patterns [22], [23], [24]. However, current investigations predominantly focus on simple displacement control of individual components, while significant challenges remain in achieving multi-DOF continuous motion, multi-structure coordination, adaptability to

Received 22 September 2025; accepted 28 December 2025. Date of publication 19 January 2026; date of current version 27 January 2026. This article was recommended for publication by Associate Editor F. Chen and Editor B. Mazzolai upon evaluation of the reviewers' comments. This work was supported in part by the National Natural Science Foundation of China under Grant 62573309 and Grant 62303340 and in part by the Natural Science Foundation of Jiangsu Province of China under Grant BK20230480. *(Corresponding authors: Xuan Li; Tao Chen.)*

Yongze Li, He Gao, and Tao Chen are with the School of Future Science and Engineering, Soochow University, Suzhou 215222, China (e-mail: chent@suda.edu.cn).

Zhiguang Xing is with the Department of Mechanical Engineering, Harbin Institute of Technology, Weihai 264209, China.

Xuan Li is with the School of Mechanical and Electrical Engineering, Soochow University, Suzhou 215137, China (e-mail: xuanli@suda.edu.cn).

This article has supplementary downloadable material available at https://doi.org/10.1109/LRA.2026.3655267, provided by the authors.

Digital Object Identifier 10.1109/LRA.2026.3655267

IEEE Robotics and Automation Letters (RA-L) paper, presented at ICRA 2026, Vienna, Austria. Cite as RA-L paper.

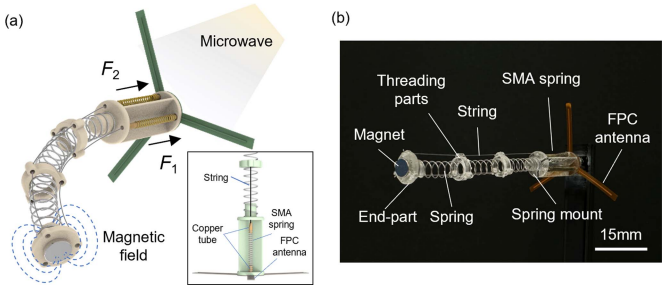

Fig. 1. (a) Schematic illustration of a microwave-driven continuum robotic arm. (b) Photo of a continuum robotic arm.

complex environments, and functional integration [25], [26], [27] through inherent properties of microwaves, such as the energy selectivity of polarization direction [28], [29]. Particularly in obstructed environments, the precise coupling between microwave-based directional energy control and mechanical motion remains a challenge.

This paper proposes a non-contact continuum robotic arm operation strategy based on microwave-driven actuation with polarization direction guidance. By integrating specifically designed FPC antennas with spatial microwave energy field distribution modulation, the system achieves contactless actuation and motion control of the robotic end-effector (Fig. 1(a)). The multi-DOF motion regulation is accomplished through spring-supported structures and SMA spring deformation responses, enabling obstacle penetration and operational capabilities (e.g., grasping and retrieval of fallen components) without physical connections. This methodology presents a novel contactless multi-DOF and multi-structure driving solution for robotic operations behind obstacles or within confined spaces, significantly enhancing the robotic arm's operational potential and application scope in unstructured environments.

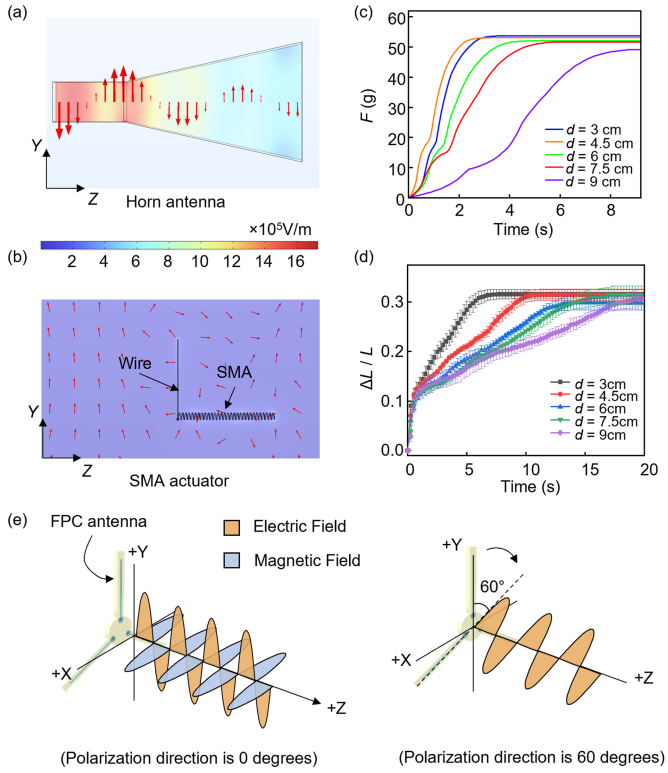

Fig. 2. (a) Simulated radiation pattern of a horn antenna, with the red arrows representing the electric field vectors. (b) Simulated microwave electric field distribution around the actuator. (c) Relationship between the pulling force F of the SMA actuator and the distance d from the wave port under fixed parameters (the microwave power $P = 42$ W, number of SMA spring coils $n_{\mathrm{SMA}} = 30$, and antenna length $l_{\mathrm{w}} = 15$ mm). (d) The relationship between the contraction ratio of the SMA spring and the distance from the waveguide port, where L represents the original length of the SMA spring, and ΔL denotes the spring contraction amount. The parameters were fixed at $P = 42$ W, $n_{\mathrm{SMA}} = 30$, and $l_w = 15$ mm. The error bars in the graph represent the standard deviation of five independent experiments. (e) Reception efficiency modulation of FPC antenna via polarization direction tuning.

II. System Modeling

A. Actuator Characteristics and Control Mechanisms

Fig. 1(b) illustrates the structure of the microwave-driven continuum robotic arm, which primarily consists of a spring-based backbone, threading parts, an end-part, a magnet, strings, SMA spring actuators, a FPC antenna, and a spring mount. The spring-based backbone and SMA springs are fixed onto the spring mount, while the threading parts are secured to the exterior of the spring-based backbone. The top ends of the SMA springs are connected to the strings via copper tubes, and the strings pass through the spring mount and threading parts before being anchored to the end-part. A disk-shaped magnet is mounted on the end-part. The opposite ends of the three SMA springs are connected to the FPC antenna through copper tubes. The FPC antenna is responsible for receiving spatial microwave energy and converting it into driving current, which is transmitted to the SMA springs. The SMA springs utilize the Joule heating effect to achieve a martensite-to-austenite phase transformation, thereby generating tensile force on the strings. The SMA spring is made of nickel-titanium alloy, with a wire diameter of 0.2 mm, an inner diameter of 1 mm, and 30 coils. Its phase transition temperature ranges from 40 to 60°C. It contracts upon heating and returns to its original shape upon cooling.

The microwave source employs a pyramidal horn antenna. The electromagnetic simulation results of the horn antenna for driving the continuum robotic arm are presented in Fig. 2(a). The dimensions of the horn's wave port were 80 × 60 mm, and the waveguide measured 40.2 × 20.2 mm. The background color-graded cloud map illustrates the spatial electric field intensity distribution, while the red arrows represent the direction of the electric field vectors. The simulation results clearly demonstrate a directional radiation beam generated by the antenna under excitation of the dominant mode (TE_{10} mode), with its maximum radiation direction extending along the antenna axis. The polarization direction of the electric field vectors is perpendicular to the antenna's base plane. This microwave mode achieves directional energy convergence through an asymmetric field distribution, providing a forward radiation field with controllable direction and concentrated energy for driving the continuum robotic arm.

Fig. 2(b) illustrates the electric field distribution surrounding the SMA actuator, where the arrow lengths represent normalized

IEEE Robotics and Automation Letters (RA-L) paper, presented at ICRA 2026, Vienna, Austria. Cite as RA-L paper.

electric field intensity. In the space, the polarization direction aligns with the Y-axis, while in the vicinity of the wire, the electric field vectors orient perpendicular to the wire surface. According to the geometric configuration of the continuum robotic arm's components, the wire direction coincides with the polarization direction, enabling it to function as a receiving antenna for the actuator. The monopole antenna was designed with a resonant length of 13 mm, corresponding to a quarter-wavelength at the operational microwave frequency of 5.8 GHz. The SMA spring axis remains perpendicular to the polarization direction, thus remaining inactive to microwave energy reception. Consequently, the wire converts incident microwave energy into electrical energy, which is subsequently transformed into thermal energy via the Joule heating effect within the SMA spring, ultimately providing mechanical actuation through the shape memory effect.

Fig. 2(c) reveals the quantitative relationship between the pulling force (F) of the SMA actuator and the distance (d) from the waveguide port. The tensile force sensor is a Jinno high-precision S-type load cell model JLBS-M2 with a range of 0∼0.5 kg. The sensor is connected to the SMA spring via a cord. The maximum force reaches 50 g with the most rapid decay rate at distances ranging from d = 3∼4.5 cm. When the distance increases to d = 9 cm, the peak force decreases below 50 g with significantly attenuated decay kinetics. All curves exhibit exponential relaxation behavior, indicating that the microwave energy transfer efficiency follows an inverse-square law with distance, consequently resulting in a reduction of the phase-transformation-driven actuation force with increasing separation. As can be seen from Fig. 2(c), the SMA spring can generate a reliable tensile force (approximately 38 g) within about 1.5 s of microwave actuation. The relationship between the contraction ratio ($\Delta L/L_0$) of the SMA actuator and d is shown in Fig. 2(d). The contraction ratio reaches 30% within 7 seconds at d = 3 cm, while the contraction rate exhibits significant attenuation with increasing distance (refer to Movie S1).

The directional control mechanism of polarization orientation on the reception efficiency of the FPC antenna is illustrated in Fig. 2(e). The monopole antennas on the FPC substrate are arranged with a 120° angular separation between adjacent elements. When the polarization angle is set to 0°, the antenna exhibits maximum radiation lobe along the Y-axis direction, while the reception efficiency of the other two monopole antennas are

$$\eta = \cos^2 \Delta\tau \tag{1}$$

where, $\Delta\tau$ is the polarization mismatch angle. Under this configuration, the polarization mismatch angle between the other two monopole antennas and the spatial microwave field $\Delta\tau$ = 60°, resulting in an efficiency reduction to one-quarter of the fully polarized-matched state. When the polarization direction is adjusted to 60°, the gain distribution in the Y-X plane undergoes reconstruction, thereby altering the microwave reception efficiency of each monopole antenna. Therefore, to ensure adequate isolation, the minimum angular separation is 60° (which yields equivalent projection effects on the circumference as 120°).

Precise control of the incident wave's polarization vector direction enables programmable reconfiguration of the spatial gain distribution of the FPC antenna, which subsequently modulates

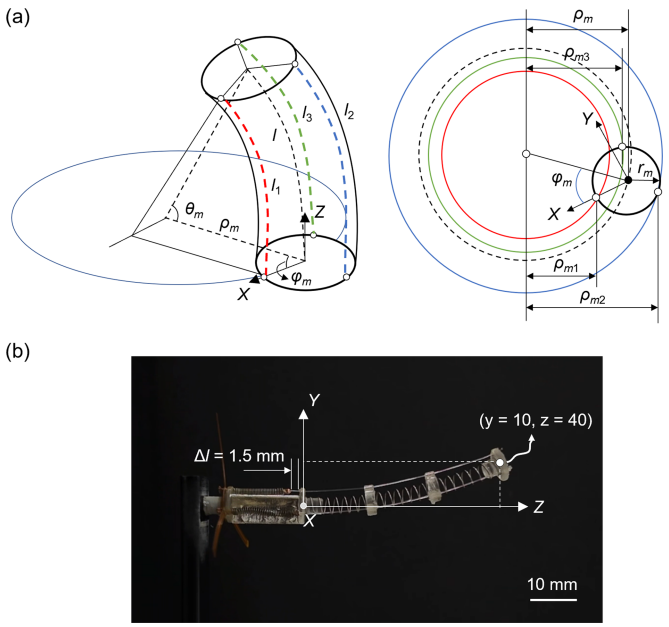

Fig. 3. (a) Model of the continuum robotic arm. (b) Robotic arm configuration under single-SMA actuation.

the actuation response of the continuum robotic arm system integrated with three actuators.

B. Constant Curvature Model

The structural schematic of the continuum robotic arm is illustrated in Fig. 3(a). The threading components are coaxially mounted along the exterior of the spring, with three strings passing through these components. This configuration is simplified as a tendon-driven spring mechanism, where the string lengths are denoted as l_1, l_2, and l_3. Differential tensile forces applied to these strings result in length variations, inducing controlled bending deformation of the spring. The X-axis is aligned with drive string 1. Based on the constant curvature model assumption illustrated in Fig. 3, the kinematic relationships among the drive space (l_1, l_2, l_3), joint space (ρ_m, θ_m, φ_m), and task space (x, y, z) are derived as follows

$$l_i = \rho_{mi}\theta_m = [\rho_m - r_m \cos(\varphi_m + \phi_i)]\theta_m \tag{2}$$

where, ρ_m (m) denotes the curvature radius of the circular arc formed by the bent robotic arm, θ_m (rad) represents the central angle of the resulting arc, φ_m (rad) indicates the torsion angle of the robotic arm, ρ_{mi} (m) denotes the vertical distance from the i-th drive string to the center of the base ring, and Φ_i (rad) is the phase angle of each driving line hole in the circumferential direction. Equation (2) can be expanded as

$$\begin{cases} l_1 = [\rho_m - r_m \cos(\varphi_m)]\theta_m ① \\ l_2 = [\rho_m + r_m \cos(\varphi_m - \pi/3)]\theta_m ② \\ l_3 = [\rho_m + r_m \cos(\varphi_m + \pi/3)]\theta_m ③ \end{cases} \tag{3}$$

where r_m represents the radius of the spring skeleton. By solving (3), we obtain

$$\tan\varphi_m = \sqrt{3}(l_2 - l_3)/(l_2 + l_3 - 2l_1), (l_2 + l_3 \neq 2l_1) \tag{4}$$

IEEE Robotics and Automation Letters (RA-L) paper, presented at ICRA 2026, Vienna, Austria. Cite as RA-L paper.

By setting$K_{\varphi_m} = \sqrt{3}(l_2 - l_3)/(l_2 + l_3 - 2l_1)$, the central axis length $l = (l_1 + l_2 + l_3)/3$, the following condition applies when l_1, l_2 and l_3 are not simultaneously equal

$$\varphi_m = \arctan 2(K_{\varphi_m}) \tag{5}$$

$$\theta_m = 2\sqrt{l_1^2 + l_2^2 + l_3^2 - l_1 l_2 - l_1 l_3 - l_2 l_3}/3r_m \tag{6}$$

Based on geometric relationships, the curvature radius of the manipulator bending is derived as

$$\rho_m = \frac{l_1 + l_2 + l_3}{3\theta_m} \tag{7}$$

Then, we obtain

$$\text{IF} l_1 = l_2 = l_3, [x, y, z]^{\mathrm{T}} = [0, 0, l_1]^{\mathrm{T}}$$

$$\text{ELSE} \begin{bmatrix} x \\ y \\ z \end{bmatrix} = \begin{bmatrix} \rho_m \cos\varphi_m(1 - \cos\theta_m) \\ \rho_m \sin\varphi_m(1 - \cos\theta_m) \\ \rho_m \sin\theta_m \end{bmatrix} \tag{8}$$

We compared the actual motion of the robotic arm with the model. The radius of the spring skeleton r_m is 2 mm, and the displacement of the SMA spring pulling the spring skeleton is approximately 2.5 mm. Based on the change in the driving wire length $\Delta l = 1.5$ mm, with $\varphi_m = \pi/2$, $l_1 = 43.5$ mm, and $l_2 = l_3 = 45$ mm, the position of the end point obtained via the constant curvature assumption is $x, y, z = (0\,\text{mm}, 10.9\,\text{mm}, 42.6\,\text{mm})$, and $\theta_m = 28.6°$. During actual testing under the conditions of $P = 42$ W and $d = 30$ mm, the spring displacement is shown in Fig. 3(b). When driving the robotic arm under identical conditions, the displacement at the end of the spring skeleton was observed to be slightly smaller ($x = 0$ mm, $y = 10$ mm, $z = 40$ mm). The main error arises from the discrepancy between the constant curvature model and the actual model. In the actual structure, the continuum robotic arm has only three wire guide rings, causing the driving wire to form three consecutive straight segments rather than a curve.

C. Non-Contact Control of Continuum Robotic Arms

The core components and signal flow of the control system for the microwave-actuated continuum robotic arm are illustrated in Fig. 4(a). The overall architecture reflects a closed-loop control logic from command input to physical actuation. An Arduino microcontroller serves as the central processing unit, responsible for receiving high-level control commands and coordinating the actions of various executive components. A stepper motor is directly connected to a horn antenna via a mechanical transmission mechanism to adjust the polarization direction of the microwave emitted by the antenna. The microwave actuation module consists of a microwave source, a relay, and a power supply. The relay acts as a high-voltage switch controlled by digital signals from the Arduino, enabling the microwave source circuit to be switched on or off as needed, thereby achieving on-demand output of microwave energy. The high-frequency electromagnetic field generated by the microwave source (42W, 5.8GHz) is transmitted through a coaxial cable to the horn antenna and emitted toward the receiving antenna embedded in the continuum robotic arm. This process utilizes thermal effects to drive flexible deformation of the continuum structure. The entire system integrates logic decision-making, motion control, and energy modulation through the Arduino, realizing a coordinated multi-module operational mechanism.

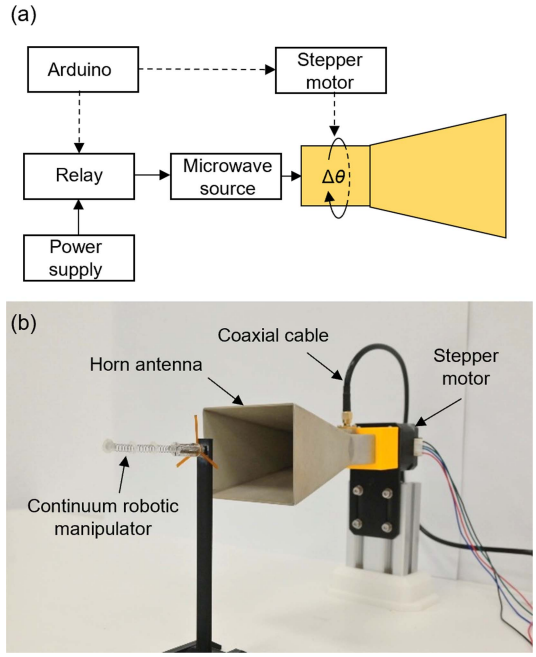

Fig. 4. (a) Schematic diagram of the control system for a microwave-actuated continuum robotic arm. (b) Photo of microwave actuation system.

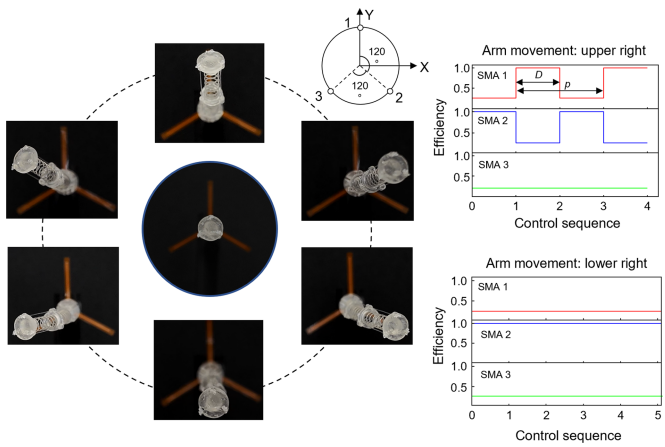

Fig. 5. Photos and control logic of a continuum robotic arm moving in different directions via microwave polarization control.

Based on the control system illustrated in Fig. 4(a), a microwave control platform was constructed (Fig. 4(b)), enabling precise manipulation of the continuum robotic arm's motion through regulation of microwave polarization direction. As shown in Fig. 5, multi-directional movement of the robotic arm—including upward, downward, upper-left, lower-left, upper-right, and lower-right—was achieved via polarization modulation. The antennas are arranged in a circumferentially uniform layout: Antenna 1 is positioned along the Y-axis, while Antennas 2 and 3 are symmetrically distributed at 120° intervals in the clockwise and counterclockwise directions, respectively.

IEEE Robotics and Automation Letters (RA-L) paper, presented at ICRA 2026, Vienna, Austria. Cite as RA-L paper.

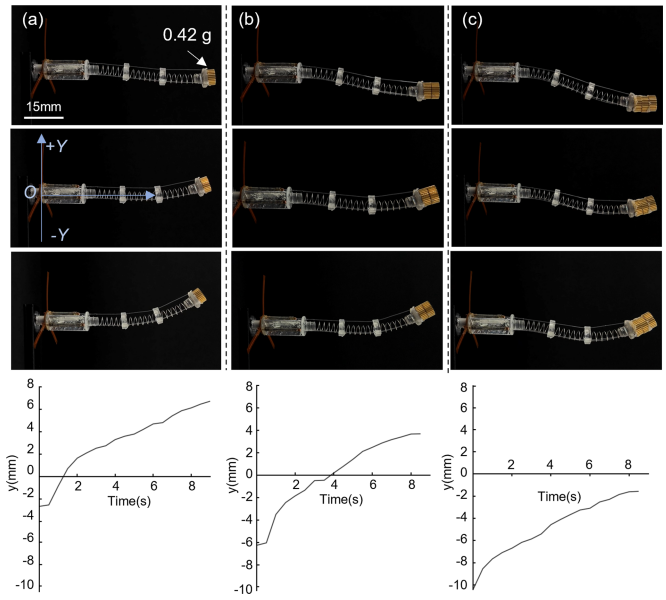

Fig. 6. Motion trajectory photos of the robotic arm end-effector under different load conditions. (a) one gear, (b) two gears, (c) three gears, with the corresponding end-effector trajectories shown below each subfigure. The parameters used in (a to c) were $P = 42$ W and $d = 30$ mm.

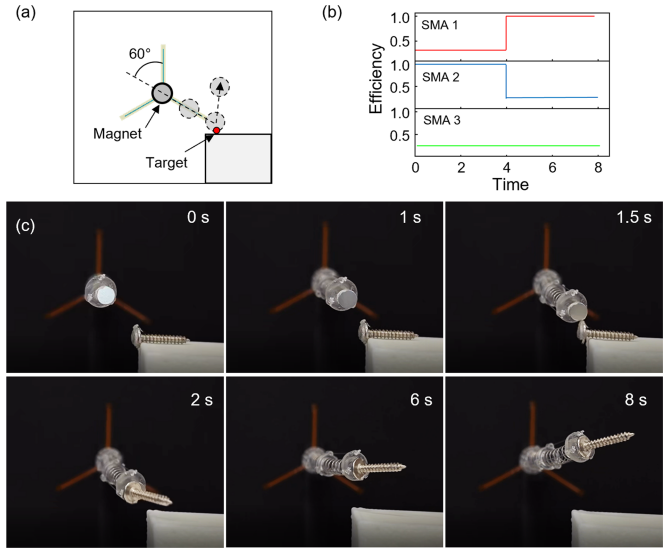

Fig. 7. (a) End-effector path of the continuum robotic arm during target part grasping. (b) Microwave reception efficiency of each SMA during the grasping process. (c) Photo of the continuum robotic arm grasping the component.

For motion toward specific antenna directions (upward, lower-left, and lower-right), a direct polarization matching strategy was employed by aligning the microwave polarization with the optimal reception polarization of the corresponding FPC antenna. Movements in other directions required a dynamic polarization modulation strategy. Taking the upper-right direction as an example, the reception efficiencies of SMA1 and SMA2 were modulated by a square wave with a period $p = 0.6$ s and duty cycle $D = 0.3$, switching between 0.25 and 1, while SMA3 maintained a constant reception efficiency of 0.25. Fine adjustment of the duty cycle allowed precise control of slight deviations in the robotic arm's trajectory. In the photograph, the horn antenna (microwave transmitting antenna) is located behind the black background at a distance of $d = 30$ mm from it. Experimental results demonstrate that this control strategy effectively achieves directional manipulation of the microwave-driven continuum robotic arm in multi-antenna collaborative operation.

III. Experiment Evaluation

A. Payload of the Continuum Robotic Arm

Fig. 6 illustrates the kinematic trajectory characteristics of the robotic arm end-effector under different gear loading conditions, corresponding to three operational scenarios: one gear (0.42 g), two gears (0.84 g), and three gears (1.26 g). Fig. 6(a) presents a photographic snapshot of the end-effector motion under light load (0.42 g). Fig. 6(b) and (c) depict the time-dependent displacement curves of the end-effector over a duration of 0∼8 seconds under varying load conditions (refer to Movie S2). As the load increases progressively, the end-effector motion exhibits notable differences in dynamic response: under the one-gear condition, the displacement profile remains relatively smooth with limited fluctuation; when the load increases to two gears, pronounced overshoot and prolonged settling time are observed; under the maximum load of three gears, the displacement persistently remains in the negative region, indicating significant steady-state deviation. These results clearly demonstrate the substantial influence of increased load on both the position and dynamic stability of the robotic arm end-effector.

B. Microwave-Controlled Grasping of Target Objects

The motion trajectory of the end-effector of the continuum robotic arm during a capture task is shown in Fig. 7(a) (refer to Movie S3). The objective was to approach a target (screw) located at the lower-right position, lift it using magnetic adsorption, and subsequently perform an upward grasping operation. Corresponding to the task requirements, the time-dependent microwave reception efficiency curves of the three shape memory alloy actuators (SMA1, SMA2, and SMA3) are shown in Fig. 7(b). SMA1 and SMA2 exhibit alternating pulse responses, while SMA3 remains relatively stable, with a cycle of approximately 8 seconds.

This efficiency modulation demonstrates independent energy allocation to each antenna via polarization control, providing the actuation basis for multi-DOF motion of the robotic arm. In the first phase, with a polarization angle of 60°, SMA2 reached polarization matching with a reception efficiency of 1, while SMA1 and SMA3 operated at an efficiency of 0.25, resulting in downward-right motion of the arm. In the second phase, under a polarization angle of 0°, SMA1 achieved polarization matching (efficiency of 1), leading to upward motion driven primarily by SMA1 and SMA2. Fig. 7(c) shows a still photograph of the robotic arm successfully grasping the target part. The image clearly captures the end-effector securely holding the metal component via a magnetic adsorption device, validating the effectiveness of the microwave-driven actuation and efficiency-coordinated control strategy in complex grasping tasks. It is

IEEE Robotics and Automation Letters (RA-L) paper, presented at ICRA 2026, Vienna, Austria. Cite as RA-L paper.

noteworthy that during the actuation process, due to the non-instantaneous heating and cooling characteristics of the SMA springs within the robotic arm, when the polarization efficiency of SMA spring 1 switches to 1 while that of SMA spring 2 becomes 0, the robotic arm cannot instantaneously reorient toward the direction of SMA spring 1. Instead, it undergoes a transitional angular change (as shown in Fig. 7), where the intermediate states are jointly determined by the current SMA status and its previous state.

IV. Conclusion

In this work, we propose and demonstrate a continuum robotic arm drive system based on microwave energy transfer and non-contact polarization control, aiming to overcome the operational limitations of conventional rigid manipulators and physically transmitted continuum mechanisms in constrained and unstructured environments. Through integrated electromagnetic simulations and systematic experimental validation, we developed an actuation scheme employing 5.8 GHz microwave as the energy carrier and achieved multi-DOF motion control via dynamic polarization modulation. The system successfully accomplished precise grasping and motion control of various small components, such as gears and screws. The cooling time of the SMA spring at room temperature typically takes about 15 s, and its actuation frequency can be accelerated by methods such as forced convective heat transfer. This study not only verifies the feasibility of microwave-driven actuation in the field of continuum robotics, but also provides a new design paradigm and technical pathway for flexible operating systems that require no physical connections and can adapt to occluded environments.

Future work will focus on multi-objective cooperative control, optimization of conformal antennas, and adaptive polarization algorithms to further enhance the operational robustness and energy utilization efficiency of the system in dynamically obscured scenarios. Furthermore, by introducing new microwave characteristics, such as frequency, the microwave-actuated system can achieve a greater degree of control freedom and enhance the functional complexity of the system. Applications in minimally invasive medical surgery and disaster response operations in narrow spaces will also be explored to promote the practical adoption of non-contact actuation technologies in soft and continuum robotics.

Acknowledgment

The authors declare no conflict of interest. All data needed to evaluate the conclusions in the paper are present in the paper and/or the Supplementary Materials.

References

[1] D. A. Haggerty et al., "Control of soft robots with inertial dynamics," *Sci. Robot.*, vol. 8, no. 81, 2023, Art. no. eadd6864.
[2] Z. Xie et al., "Soft robotic arm with extensible stiffening layer," *IEEE Robot. Autom. Lett.*, vol. 8, no. 6, pp. 3597–3604, Jun. 2023.
[3] Z. Xie et al., "Octopus-inspired sensorized soft arm for environmental interaction," *Sci. Robot.*, vol. 8, no. 78, 2023, Art. no. eadh7852.
[4] J. Ma, Z. Han, L. Yang, G. Min, Z. Liu, and W. He, "Dynamics modeling of a soft arm under the cosserat theory," in *Proc. IEEE Int. Conf. Real-time Comput. Robot.*, 2021, pp. 87–90.
[5] Z. Tian et al., "Wave number–spiral acoustic tweezers for dynamic and reconfigurable manipulation of particles and cells," *Sci. Adv.*, vol. 5, no. 5, May 2019, Art. no. eaau6062.
[6] Z. Chen et al., "Advances in micromanipulation actuated by vibration-induced acoustic waves and streaming flow," *Appl. Sci.*, vol. 10, no. 4, Feb. 2020, Art. no. 1260.
[7] S. Mohanty et al., "Acoustically-actuated bubble-powered rotational micro-propellers," *Sensors Actuators B, Chem.*, vol. 347, Dec. 2021, Art. no. 130589.
[8] Y. Xiao et al., "Acoustics-actuated microrobots," *Micromachines*, vol. 13, no. 3, Mar. 2022, Art. no. 481.
[9] E. Xue et al., "Photothermal and humidity stimulus-responsive self-sensing soft actuators for smart packaging," *ACS Appl. Polym. Mater.*, vol. 5, no. 6, pp. 4525–4535, Jun. 2023.
[10] Y. Jiang et al., "One stone, two birds: Spidroin-inspired nanogels for high-performance fibers and photothermal actuators," *Adv. Funct. Mater.*, vol. 33, no. 35, Sep. 2023, Art. no. 2303387.
[11] Y. Chen, C. Valenzuela, X. Zhang, X. Yang, L. Wang, and W. Feng, "Light-driven dandelion-inspired microfliers," *Nature Commun.*, vol. 14, May 2023, Art. no. 3036.
[12] N. P. Skillin et al., "Photothermal actuation of thick 3D-printed liquid crystalline elastomer nanocomposites," *Adv. Mater.*, vol. 36, no. 34, Aug. 2024, Art. no. 2313745.
[13] C. Wang, V. R. Puranam, S. Misra, and V. K. Venkiteswaran, "A snake-inspired multi-segmented magnetic soft robot towards medical applications," *IEEE Robot. Autom. Lett.*, vol. 7, no. 2, pp. 5795–5802, Apr. 2022.
[14] M. Sun et al., "Reconfigurable magnetic slime robot: Deformation, adaptability, and multifunction," *Adv. Funct. Mater.*, vol. 32, no. 26, Jul. 2022, Art. no. 2112508.
[15] B. Sun, "Magnetic arthropod millirobots fabricated by 3D-printed hydrogels," *Adv. Intell. Syst.*, vol. 4, no. 1, Jan. 2022, Art. no. 2100139.
[16] Z. Wang et al., "A magnetic soft robot with multimodal sensing capability by multimaterial direct ink writing," *Additive Manuf.*, vol. 61, Jan. 2023, Art. no. 103320.
[17] M. H. D. Ansari et al., "3D printing of small-scale soft robots with programmable magnetization," *Adv. Funct. Mater.*, vol. 33, no. 15, Apr. 2023, Art. no. 2211918.
[18] T. Ozaki, N. Ohta, T. Jimbo, and K. Hamaguchi, "A wireless radiofrequency-powered insect-scale flapping-wing aerial vehicle," *Nature Electron.*, vol. 4, no. 11, pp. 845–852, Nov. 2021.
[19] T. Y. Koh and A. Sutradhar, "Untethered selectively actuated microwave 4D printing through ferromagnetic PLA," *Additive Manuf.*, vol. 56, Sep. 2022, Art. no. 102866.
[20] Z. Zhao et al., "Advancements in microwave absorption motivated by interdisciplinary research," *Adv. Mater.*, vol. 36, no. 4, Jan. 2024, Art. no. 2304182.
[21] Y. Li et al., "Multi-degree-of-freedom robots powered and controlled by microwaves," *Adv. Sci.*, vol. 9, no. 29, 2022, Art. no. 2203305.
[22] S. Aziz et al., "A microwave powered polymeric artificial muscle," *Appl. Mater. Today*, vol. 23, Jun. 2021, Art. no. 101021.
[23] L. Chen, Y. Liu, and J. Leng, "Microwave responsive epoxy nanocomposites reinforced by carbon nanomaterials of different dimensions," *J. Appl. Polym. Sci.*, vol. 135, no. 9, Mar. 2018, Art. no. 45676.
[24] R. K. Gupta, S. A. R. Hashmi, S. Verma, A. Naik, and P. Nair, "Recovery stress and storage modulus of microwave-induced graphene-reinforced thermoresponsive shape memory polyurethane nanocomposites," *J. Mater. Eng. Perform.*, vol. 29, no. 1, pp. 205–214, Jan. 2020.
[25] Y. Song et al., "Navigating soft robots through wireless heating," in *Proc. IEEE Int. Conf. Robot. Autom.*, London, U.K., 2023, pp. 2598–2605.
[26] Y.-C. Wang et al., "Graphene implanted shape memory polymers with dielectric gene dominated highly efficient microwave drive," *Adv. Funct. Mater.*, vol. 33, no. 40, Oct. 2023, Art. no. 2303560.
[27] S. Ueno and Y. Monnai, "Wireless soft actuator based on liquid-gas phase transition controlled by millimeter-wave irradiation," *IEEE Robot. Autom. Lett.*, vol. 5, no. 4, pp. 6483–6488, Oct. 2020.
[28] T. Ozaki et al., "A wireless radiofrequency-powered insect-scale flapping-wing aerial vehicle," *Nature Electron.*, vol. 4, pp. 845–852, 2021.
[29] S. S. Zhong, *Antenna Theory and Techniques*, 2nd ed. Beijing, China: Publishing House of Electronics Industry, 2015, pp. 66–67.